Direct Displacement Control for Single-Winding Bearingless Switched Reluctance Motor

ZHENYANG HAO, (Member, IEEE), TAO ZHU, XIN CAO, (Member, IEEE), QIANG YU, AND QIYAO ZHANG, (Student Member, IEEE)
Department of Electrical Engineering, Nanjing University of Aeronautics and Astronautics, Nanjing 210016, China

Corresponding author: Zhenyang Hao (zhenyang_hao@nuaa.edu.cn)

ABSTRACT Although the conventional control strategy of Bearingless Switched Reluctance Motors (BSRMs) can realize stable suspension of the motor shaft, it still has disadvantages such as relying on the model calculation, strong coupling between torque and displacement, and poor anti-interference ability. In order to solve these problems, this paper studies a direct displacement control (DDC) strategy for single-winding BSRMs (SWBSRMs). This strategy draws on the control idea of magnetic bearings, and realizes the stable suspension of BSRMs on the premise of separating from the mathematical model online calculation. At the same time, the strategy realizes the decoupling of torque and suspension displacement, and has good anti-disturbance. Finally, experimental results show that compared with the conventional control strategy and DTC and DFC method, the DDC strategy reduces the execution time of the algorithm by 36.6% and 41.2% during steady-state; reduces the speed-up time by 60% and 23% during dynamic conditions; and reduces the speed-down time by 20% and 86.6%.

INDEX TERMS Bearingless switched reluctance motor, direct displacement control, mathematical model, decoupling.

I. INTRODUCTION

Because the switched reluctance motor (SRM) employs centralized windings and has no windings and permanent magnets on its rotor, it has the advantages of low cost, simple structure, flexible control, and strong fault tolerance. Therefore, SRMs have been paid more attention to different applications [1]–[5]. Bearingless motor technology uses magnetic levitation to separate the rotating shaft of the conventional motor from the bearing. It has the advantages of low friction loss, high efficiency, and high speed adaptability [6]. In recent years, BSRMs have been proposed and developed to further improve the high-speed adaptability of conventional SRMs [7]–[9].

In [10], a square wave current control strategy for BSRMs was proposed in which the winding current was calculated based on the mathematical model of torque and levitation force. In [11], the average torque and levitation force were taken as control targets, and the average torque in the levitation area was kept at zero. By adjusting the turn-on angle to change the torque, independent control of torque and

levitation force was achieved, but there was still a problem of large fluctuations in torque and levitation force. In [12], the author takes the reduction of torque ripple and suspension force fluctuation as the goal, and combines the analytical model with a multi-objective genetic particle swarm optimizer. The current waveform is optimized on the basis of the independent control strategy, which effectively reduces torque ripple and suspension force fluctuation. With the development of direct torque control (DTC) in SRMs, direct torque control and direct force control strategy (DTC & DFC) was proposed for BSRMs. The strategy takes torque and levitation force as the control targets. By selecting the voltage vector to control the increase and decrease of torque and levitation force, the ripple of torque and levitation force can be significantly reduced. However, some voltage vectors will generate excessive negative torque, which will increase the copper loss and decrease the torque-current ratio [13]–[16]. In [17], a direct instantaneous torque and direct force control (DITC & DFC) strategy was proposed, which eliminates the active control of the magnetic flux-linkage to simplify the control strategy, and can also reduce the torque ripple. In [18], the suspension force compensation measures for BSRMs winding short circuit were proposed, which further

---

The associate editor coordinating the review of this manuscript and approving it for publication was Jonghoon Kim.

improved the fault tolerance of the motor. However, there is still a large torque ripple. In [19], a coordinated control strategy based on the adjustable turn-off angle is proposed. The main winding is turned off with a delay to compensate the torque, and the simulation results verify the feasibility of reducing torque ripple. Regardless of whether the above control method takes electric current or torque and levitation force as control targets, it needs to be solved by a mathematical model of torque and levitation forces. The torque and displacement are generally coupled and the control algorithm is more complicated. In [20], from the perspective of the motor structure optimization, a 12/4 pole BSRM is proposed by changing the number of rotor poles. According to the inductance curve, the torque and the suspension force are provided in different areas, so as to realize the decoupling of the two and simplify the control. In [21], a BSRM with a dual stator and segmented rotor structure is proposed. The motor runs under a short magnetic flux path, and the magnetic flux path is isolated between the torque and the suspension system. Therefore, the coupling problem of BSRM torque and suspension force is optimized.

In the conventional control method, the relative tooth current difference needs to be calculated by (5) and (6). In the DTC and DFC method, the torque and suspension force also need to be obtained by (4)-(6). These two methods need to establish the mathematical model of BSRM, and then obtain the relevant expressions, and finally can control the torque and the suspension force at the same time. In order to solve the above problems, this paper employs the control principle of magnetic bearings to study a direct displacement control (DDC) strategy for single-winding BSRMs [22]–[24]. This control strategy not only completely removes the model online calculation, but also realizes the decoupling of torque and suspension displacement, and also has good performance on the anti-disturbance ability.

The rest of the paper is organized as follows. In Section II, the levitation principle, mathematical model, conventional control strategy and DTC and DFC method of single-winding BSRMs are introduced. The working principle of the proposed DDC strategy is explained in Section III. In addition, the selection of DDC strategy parameters and system stability analysis are also introduced. Experimental results are provided in Section IV, and conclusions are made in Section V.

II. OPERATION PRINCIPLE OF SWBSRM

A. LEVITATION PRINCIPLE

Fig. 1 shows the structure of the 12/8 single-winding BSRM. Taking phase A as an example, the windings mounted on its four stator poles A1, A2, A3, and A4 are controlled by independent power converters respectively. By controlling winding A1 and winding A3 be conducted with different currents, a levitation force in the direction of α axis is generated. By controlling winding A2 and winding A4 be conducted with different currents, a levitation force in the direction of the β axis is generated. For example, when $i_{a1} > i_{a3}$, the
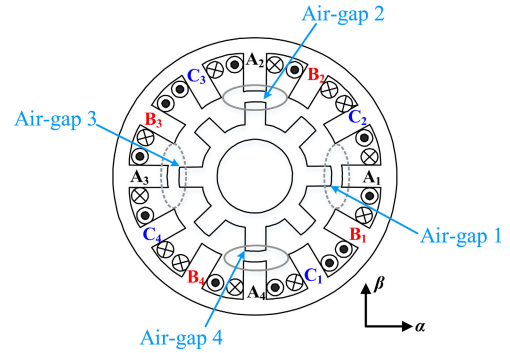

FIGURE 1. The structure of the 12/8 SWBSRM.

magnetic density at air-gap 1 is greater than the magnetic density at air-gap 3, generating a levitation force along the positive direction of α axis. Similarly, when $i_{a2} > i_{a4}$, a levitation force is generated along the positive direction of the β axis.

B. MATHEMATICAL MODELS OF TORQUE AND LEVITATION FORCE

The two control objectives of BSRMs are torque and levitation force. In order to better reveal mathematical relationships between torque, levitation force and winding current, the mathematical model between these three needs to be established. In the SWBSRM, since the stator pole winding currents of each phase are controlled separately, the mutual inductance between the windings will affect the radial levitation force. Therefore, this paper uses the virtual work method to obtain the mathematical model of torque and levitation force [18]. Under the condition of neglecting the magnetic saturation and leakage flux, the expressions of torque and levitation force can be obtained from [18]. Levitation forces in α and β directions are related to the winding currents on the four stator poles of each phase. In order to reduce the control variables and simplify the control algorithm, let

$$I_m = \frac{i_{a1} + i_{a3}}{2} = \frac{i_{a2} + i_{a4}}{2} \qquad (1)$$

$$\Delta i_\alpha = \frac{|i_{a1} - i_{a3}|}{2} \qquad (2)$$

$$\Delta i_\beta = \frac{|i_{a2} - i_{a4}|}{2} \qquad (3)$$

I_m is the average exciting current; Δi_α is the current difference in α direction, and Δi_β is the current difference in β direction. As derived in [18], the expressions of torque and levitation forces can be written as:

$$T = J_t(\theta)N^2(2I_m^2 + \Delta i_\alpha^2 + \Delta i_\beta^2) \qquad (4)$$

$$F_\alpha = 4K_{f1}(\theta)N^2 I_m \Delta i_\alpha \qquad (5)$$

$$F_\beta = 4K_{f1}(\theta)N^2 I_m \Delta i_\beta \qquad (6)$$

T is the electromagnetic torque generated when the A phase is on, and F_α and F_β are the levitation forces in α and β directions when the A phase is on. $J_t(\theta)$ and $K_{f1}(\theta)$

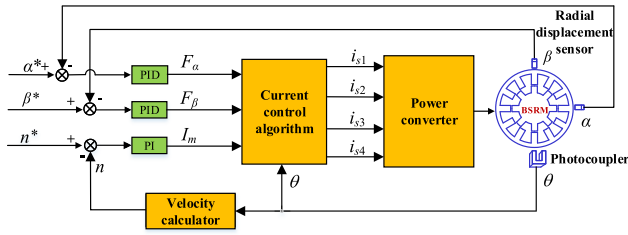**FIGURE 2. Control block of the conventional control method.**

FIGURE 3. Control block of the DTC and DFC method.

are the torque and levitation coefficients, respectively. And they are related to the position angle θ. N is the number of winding turns.

C. CONVENTIONAL CONTROL METHOD IN THIS PAPER

Fig. 2 shows the control block of the conventional control method of the 12/8 pole SWBSRM. Firstly, the speed error can be obtained from the required speed and the actual speed. And it is regulated by the PI controller to get the reference torque. The given displacement values of α^* and β^* are always zero to ensure that the real radial displacements of shaft can be regulated around its geometric-center position. At the same time, the displacement errors are regulated by the PID controllers to obtain the required levitation forces in α and β directions. Secondly, the reference currents of the four pole windings are obtained by the current control method. Finally, the required current is compared with the actual current in a hysteresis loop to control the actual torque and levitation force. The current differences Δi_α and Δi_β can be solved by (5) and (6). Then add and subtract them to the average excitation current I_m to get the reference current of the four pole windings.

Although the conventional control method can realize stable rotation and suspension of the 12/8 pole SWBSRM, it also has some disadvantages. Firstly, the control strategy needs to be calculated online using a mathematical model. The rotor cannot be suspended without the use of model analysis. Secondly, the conventional control strategy has poor dynamic stability. When the motor performs a speed change or variable load experiment, the average excitation current of each phase winding will change suddenly. This results in sudden changes in the suspension force and fluctuations in radial displacement. Even the rotor may hit the auxiliary bearing, and fails to be suspended. The suspension performance of the motor is greatly affected.

D. DTC AND DFC METHOD

The control block of the DTC and DFC control method of the 12/8 pole single-winding BSRM is shown in Fig. 3. First, the given torque is obtained through the PI controller from the difference between the given speed and the actual speed. Secondly, the calculated actual flux linkage and actual torque are respectively different from the given flux linkage and the given torque, and the corresponding increase and decrease signals are obtained through the hysteresis comparator.
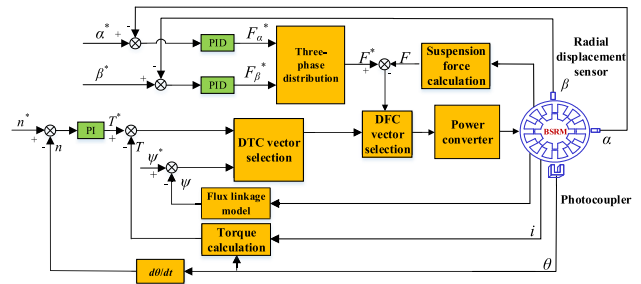
The signals are combined with the sector corresponding to the flux linkage angle to select the corresponding basic voltage vector. And then the basic voltage vector is combined with the suspension force hysteresis signal and decomposed into an equivalent voltage vector. Finally, the current of each pole winding is controlled by the power converter to realize the control of torque and levitation force.

III. PROPOSED DDC METHOD FOR SWBSRM

A. SPEED CONTROL ALGORITHM

The conventional control strategy is to control the speed by controlling the average excitation current I_m. However, the inertia of the average excitation current I_m and the winding current difference ΔI are both small. When both of them change at the same time, the system is difficult to be stable. Therefore, other variables are needed to control the speed in DDC strategy. The change of the speed reflects the change of the torque. To make the speed stable, the torque must be stabilized. Next, we analyze the torque expression. According to [10], the concept of advanced angle θ_m can be introduced here, and the conduction region of the motor phase current can be adjusted by adjusting the advanced angle. We set the length of the conduction region to 15 °, so that the turn-on angle θ_{on} and the turn-off angle θ_{off} can be expressed as

$$\theta_{on} = -\frac{\pi}{24} - \theta_m \qquad (7)$$

$$\theta_{off} = \frac{\pi}{24} - \theta_m \qquad (8)$$

The average torque T_{avg} of each phase of the 12/8 pole SWBSRM in one cycle can be obtained by integrating the instantaneous torque, which can be written as

$$T_{avg} = \frac{12}{\pi} \int_{-\frac{\pi}{24} - \theta_m}^{\frac{\pi}{24} - \theta_m} T d\theta \qquad (9)$$

In order to reduce the variables, the torque formula T can be simplified. By combining (5) and (6) and substituting them into (4), we can get

$$T = J_t(\theta) N^2 (2I_m^2 + \frac{F^2}{16K_{f1}(\theta)^2 N^4 I_m^2}) \qquad (10)$$

where F is the radial force combined by the suspension forces in the directions of α and β. Finally, substituting (7), (8),

and (10) into (9), we get

$$T_{avg} = \frac{12}{\pi} \int_{-\frac{\pi}{24}-\theta_m}^{\frac{\pi}{24}-\theta_m} J_t(\theta)N^2(2I_m^2 + \frac{F^2}{16K_{f1}(\theta)^2N^4I_m^2})d\theta$$

$$= G_{tm}(\theta_m)I_m^2 + G_{ts}(\theta_m)\frac{F^2}{I_m^2} \qquad (11)$$

where $G_{tm}(\theta_m)$ and $G_{ts}(\theta_m)$ are functions related to the lead angle θ_m, respectively. It can be seen from (11) that the average torque of the motor is related to the advanced angle θ_m, the average exciting current I_m, and the radial composite force F. When the motor shaft and load are determined, the radial composite force F is a constant. Fig. 4 shows the principle of the advanced angle control under the DDC method. Therefore, in order to control the average torque T_{avg} of the motor, it can be achieved by controlling the advanced angle θ_m under the condition that the average excitation current I_m is constant. In addition, because the advanced angle is updated once per cycle, the average levitation force in a single cycle is only related to the current difference Δi. This achieves the decoupling of torque and levitation to a certain extent.
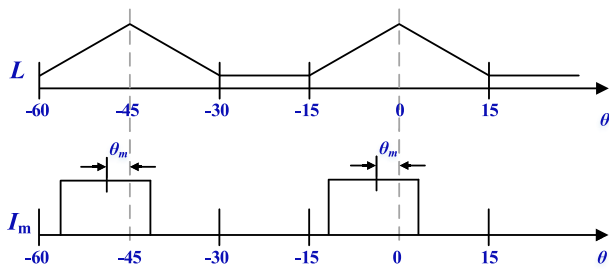

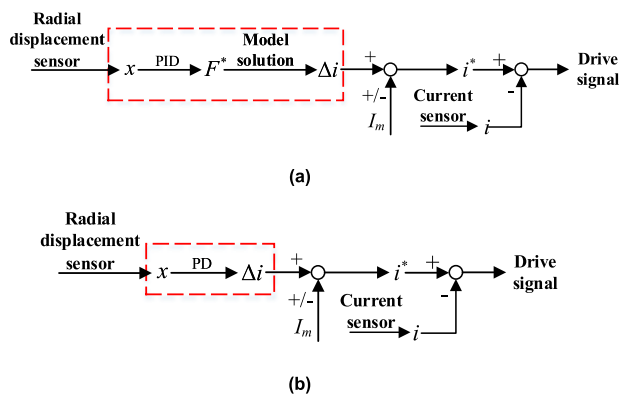**FIGURE 4.** Schematic diagram of the advanced angle control under the DDC method.

FIGURE 5. Block diagram of the displacement control. (a) conventional control method. (b) DDC method.

B. DISPLACEMENT CONTROL OF ALGORITHM

Fig. 5 shows diagrams of displacement control under the conventional control method and the DDC method. Under the conventional control method, the displacement signal outputs

a reference force after regulating by the PID controller, firstly. Then the mathematical model is used to calculate the relative difference Δi of the relative pole winding current in α/β direction. And then calculate it with the average excitation current I_m to obtain the given current of each pole winding in each phase. Finally, the switching signal is obtained through the hysteresis comparator. The entire displacement control process of the conventional control method is shown in Fig. 5(a). Under the DDC method, compared with the conventional control method, the main change is that the displacement signal regulated by the PD controller directly outputs the current difference Δi of the relative pole winding. The intermediate process does not need to undergo a required force conversion. The entire displacement control process of the DDC method is shown in Fig. 5(a). Comparing Fig. 5(a) and Fig. 5(b), it can be seen that the DDC method does not need to use a mathematical model for online calculation in displacement control. Similar to the magnetic bearing control, a simple PD controller is used to obtain the current difference Δi. This makes the displacement control no longer subject to various constraints of the mathematical model, and the stability of the control is greatly improved.
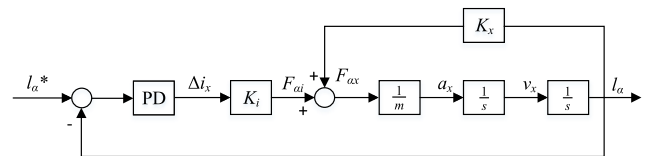

FIGURE 6. Block Diagram of displacement closed-loop control system.

C. CHARACTERISTICS OF DISPLACEMENT CLOSED-LOOP CONTROL

The structure of BSRMs' displacement closed-loop control system is basically similar to that of magnetic bearings, as shown in Fig. 6. The input is the displacement of the suspension center point l_α^*. Make a difference between it and the actual eccentricity distance l_α and regulate the difference by a PD controller. The output is the current difference of the relative pole Δi_x. The current difference is multiplied by the current stiffness coefficient K_i to obtain the corresponding radial force $F_{\alpha i}$. The eccentric distance $l\alpha$ is multiplied by the displacement stiffness coefficient K_x to obtain the corresponding radial force $F_{\alpha x}$. The two radial forces are then added to obtain a combined radial force F_α. The combined radial force is integrated twice to obtain the actual displacement.

From the above block diagram, we can obtain the transfer function and characteristic root of the displacement closed-loop control system, as shown in (12) and (13).

$$\phi_x = \frac{l_\alpha}{l_\alpha^*} = \frac{K_i(K_p + K_d s)}{ms^2 + K_i K_d s + (K_i K_p - K_x)} \qquad (12)$$

$$s = \frac{-K_i K_d \pm \sqrt{K_i^2 K_d^2 - 4m(K_i K_p - K_x)}}{2m} \qquad (13)$$

It can be seen that the characteristic equation has two different characteristic roots. The controller parameters K_p and K_d will affect the distribution of the characteristic roots, and then affect the stability of the entire closed-loop control system. Therefore, these two parameters need to be studied. First, we roughly determine the range of their values when the system is stable. When $K_p \geq K_x / K_i$ and $K_d > 0$, the closed-loop eigenvalues are shown in (14).

$$s_1, s_2 = \frac{-K_d K_i \pm \sqrt{(K_d K_i)^2 - 4m(K_i K_p - K_x)}}{2m} \quad (14)$$

It can be seen that both eigenvalues are located in the negative half-plane of the complex plane, so the closed-loop system is in a stable state.

Because the turning frequency of the open-loop transfer function is increasing gradually in the process of $-7.5° \sim 0°$ rotor movement, and the phase margin is also increasing with the rotor movement after the introduction of a PD controller. As long as K_p and K_d when θ is $-7.5°$ satisfy the phase margin greater than 30 °, the subsequent phase margin must also be greater than 30 °. Therefore, it is only necessary to analyze the closed-loop transfer function of the displacement control when the rotor position angle θ is $-7.5°$. Fig. 7 shows the schematic diagram of the K_p and K_d parameter ranges when $\theta = -7.5°$, where the x and y axes represent the range of K_p and K_d values, respectively, and the z axis represents the phase margin. First, according to the approximate range of K_p and K_d parameters determined by the above stability analysis, $K_p \geq 16000$ and $K_d > 0$ can be obtained. Then, based on this condition, observe that K_p and K_d satisfy the phase margin in the range of $30° \sim 60°$, and determine the final ranges of K_p and K_d.
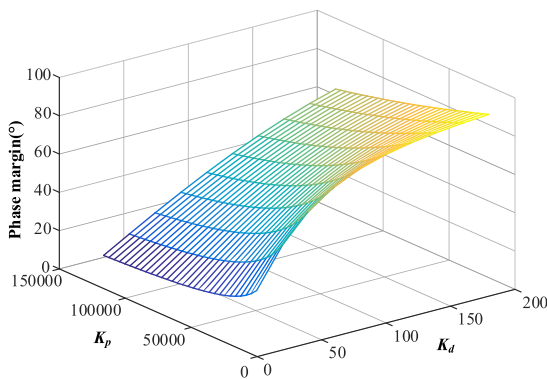

FIGURE 7. Schematic diagram of the K_p and K_d parameter range.

After continuous debugging and simulation, when $K_p = 100000$ and $K_d = 100$ are taken, the phase margin is suitable at any position of the rotor. Under this set of parameters, the Bode plot of the displacement closed-loop control system is shown in Fig. 8. The red curve represents the curve of the PD controller, with a slope of $+20$dB/dec after turning frequency; the blue curve represents the curve of the system before correction, with a slope of -40dB/dec after

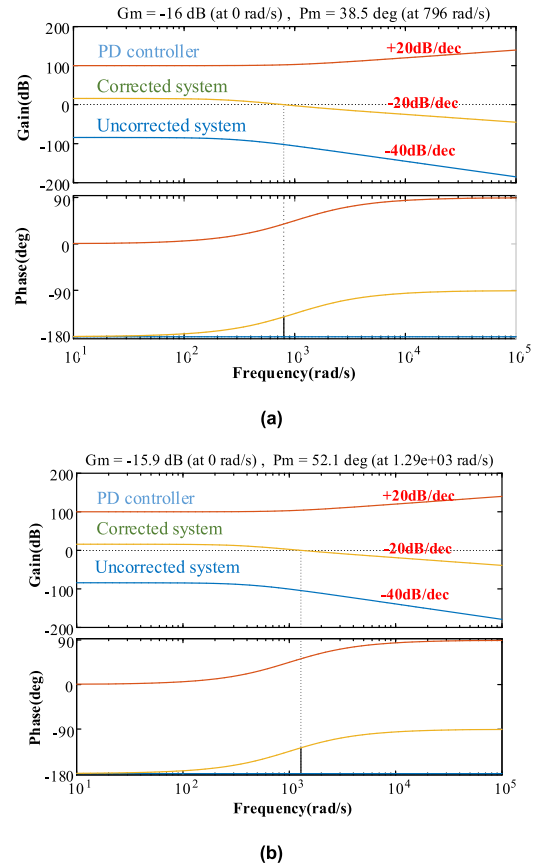**FIGURE 8.** Bode plot of the displacement closed-loop control system when $K_P = 100000$ and $K_d = 100$. (a) $\theta = -7.5°$. (b) $\theta = 0°$.

turning frequency; the yellow curve represents the curve of the system after correction, with a slope of -20dB/dec after turning frequency. In addition, by introducing a differential regulator, the system phase is no longer constant at $-180°$, the phase margin is $38.5°$ when the rotor position angle is $-7.5°$, and the phase margin is $52.1°$ when the rotor position angle is $0°$. These can indicate that the closed-loop control system performs well when the rotor is located at any position within the region providing the levitation force.

D. SELECTION PRINCIPLE OF AVERAGE EXCITATION CURRENT

In the dual-winding BSRM, there are two sets of windings on each stator pole, one is the main winding and the other is a floating winding. The main winding current is mainly used to control the torque, while the floating winding current is used to control the levitation force. The two are controlled independently, making the control algorithm of the dual-winding BSRM more simple and convenient. However, in SWBSRMs, there is only one set of windings on each stator pole. In order to make the SWBSRM control method equivalent to the dual-winding BSRM, the current on each set of windings can be divided into two parts. One part is the average excitation current I_m, which can be equivalent

to the main winding current in the dual-winding BSRM; the other part is the relative pole current difference Δi_x and Δi_y, which can also be equivalent to the floating winding current in the dual-winding BSRM. Therefore, the average excitation current I_m has two main functions in the SWBSRM control, one is to provide the electromagnetic torque of the motor rotation, and the other is to provide the bias magnetic field required for the rotor suspension. That is to say, the value of average excitation current I_m is related to motor torque and suspension force. Therefore, these two factors need to be considered comprehensively.

According to the average torque expression of (11), it can be rewritten as an expression about the average exciting current I_m, as shown in (15).

$$I_m = \sqrt{\frac{T_{avg} \pm \sqrt{T_{avg}^2 - 4G_{tm}(\theta_m)G_{ts}(\theta_m)F^2}}{2G_{tm}(\theta_m)}} \quad (15)$$

The average exciting current I_m is related to the average torque T_{avg} of the motor, the advanced angle θ_m, and the combined radial force F, as shown in (15). To determine the value of the average exciting current, the relationship between these quantities must be studied. Fig. 9(a) shows the relationship between I_m, T_{avg}, and F when $\theta_m = 7.5°$. At this time, the average torque generated by the motor is the largest. When the provided levitation force F is constant, the average exciting current I_m increases as the required torque increases. When both the rotational load component and the radial load component are determined, the minimum average exciting current can be determined from Fig. 9(a). Fig. 9(b) shows the relationship between I_m, θ_m, and T_{avg} when $F = 10N$. At this time, the radial load component is constant. It can be seen that as the advanced angle θ_m or the average exciting current I_m increases, the average torque T_{avg} increases. According to this figure, under the condition of constant radial load, the average exciting current can be determined by the rotational load component and the advanced angle. The determined current must meet the conditions of Fig. 9(a). Fig. 9(c) shows the relationship between T_{avg}, θ_m, and F when $I_m = 1A$. After determining the average exciting current through Fig. 9(a) and Fig. 9(b), use this chart to determine whether the exciting current can meet the load requirements.

E. CONTROL BLOCK OF THE DDC METHOD

Fig. 10 shows the control block of the DDC method of a 12/8 pole SWBSRM. First of all, consistent with the conventional control strategy, the speed error is input to the PI controller, but the output in DDC is the advanced angle θ_m. And the conduction region of each phase is adjusted by the advanced angle. Then, the errors of displacements in two directions are regulated by PD controllers. The output also changed from the required levitation force to the current difference. Then calculate with the average excitation current I_m, so as to obtain the given current of the four sets of windings in each phase. Finally, the power converter is used to control the levitation force and torque.
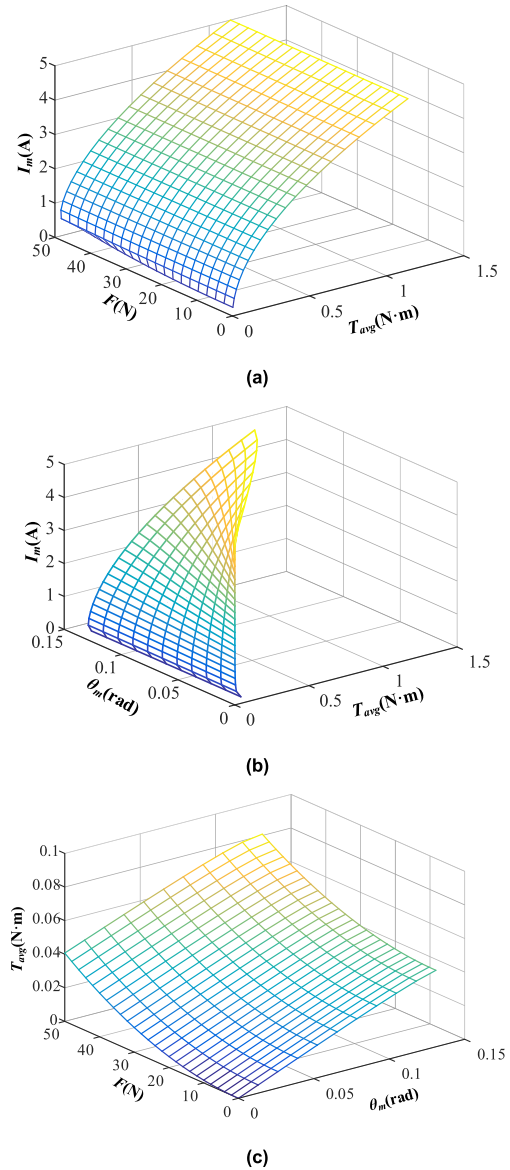

(a)

(b)

(c)

FIGURE 9. Method for determining the average exciting current. (a) The relationship between I_m, T_{avg}, and F when $\theta_m = 7.5°$. (b) the relationship between I_m, θ_m, and T_{avg} when $F = 10N$. (c) the relationship between T_{avg}, θ_m, and F when $I_m = 1A$.
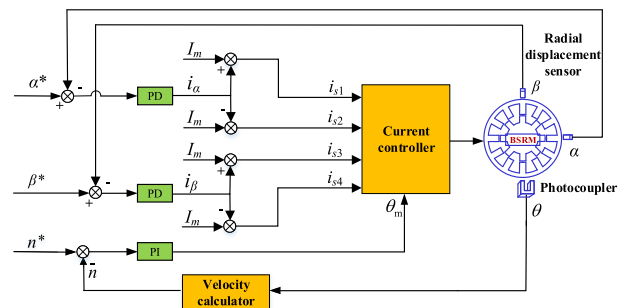

FIGURE 10. Control block of the DDC method.

IV. EXPERIMENTAL RESULTS

In order to verify the proposed DDC method, some experiments were performed on the test bench of a 12/8 pole

TABLE 1. Parameters of the experiment prototype

| Parameters	Values
Number of turns of the first winding (used in this paper)	60 turns
Number of turns of the second winding	17 turns
Rated power of the first winding	0.5kW
Rated current of the first winding	5A
Rated power of the second winding	1.5kW
Rated voltage of the motor	100V
Rated average radial force	50N
Arc angle of rotor and stator teeth	15°
Outside diameter of stator core	123 mm
Inside diameter of stator pole	54 mm
Radius of rotor pole	26.75mm
Stack length lamination	55 mm
Average air-gap length between rotor and stator	0.25 mm
Average air-gap length between shaft and backup bearing	0.2mm
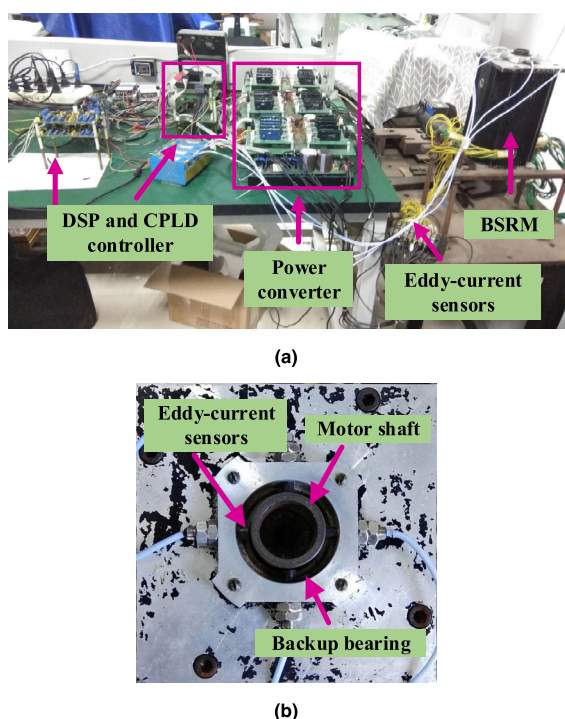
FIGURE 11. Pictures of the test bench of a 12/8 SWBSRM. (a) The experiment prototype and its control circuit. (b) Enlarged view of the motor shaft and the auxiliary bearing.

SWBSRM, as shown in Fig. 10. The parameters of the prototype are listed in Table 1. Fig. 11(a) shows the SWBSRM prototype and its control circuit. To avoid collision with the stator when the rotor is suspended, an auxiliary bearing is installed inside the motor. The radial clearance of the auxiliary bearing is 0.2mm, which is less than the length of the air-gap between the stator and the rotor by 0.25mm. The control circuit consists of the three-phase power converters, the DSP controller, current and displacement sampling, etc. The control algorithm is programmed in a TI TMS320F2812 controller. The displacements of the shaft at the direction of α axis and β axis are measured by eddy current sensors. Photoelectric sensors

are used to judge the position of the motor rotor. Fig. 11(b) shows an enlarged view of the motor shaft and the auxiliary bearing. When the motor rotor is not suspended, the auxiliary bearing rotates with the rotor; when the motor rotor is normally suspended, the auxiliary bearing is stationary, so it can be used to determine whether the motor rotor is suspended. The PI controller parameters of speed loop are adjusted online in the software, and the PID controller parameters of radial-displacement loop are adjusted by changing the resistance value in the analog operational amplifier circuit.
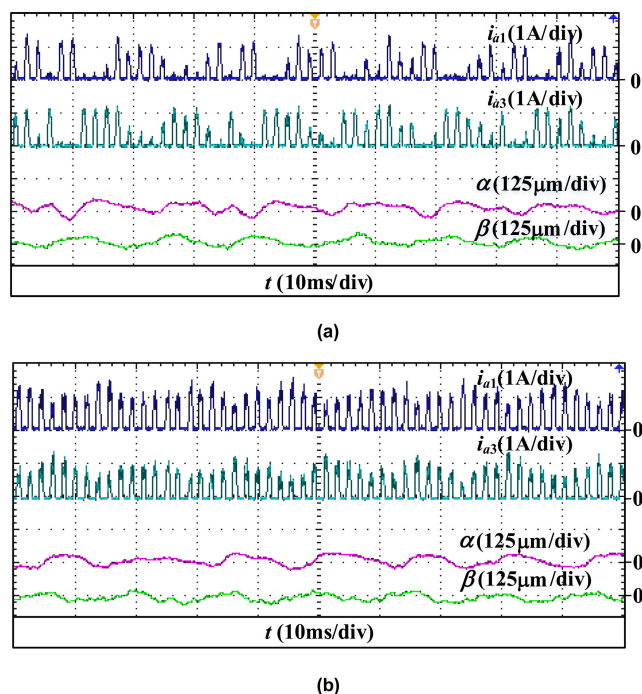

FIGURE 12. Experimental waveforms of winding currents and radial displacements. (a) Conventional control method. (b) DDC method.

A. STEADY-STATE PERFORMANCE WITH THE CONVENTIONAL CONTROL METHOD AND THE DDC METHOD

Fig. 12 shows experimental waveforms of winding currents and radial displacements at the speed of 4000 r/min with different methods. Under the conventional control method, the displacement fluctuations in α and β directions are ± 35 μm, which is far shorter than the 250 μm air gap length of one side of the motor, and the suspension performance is good. Under the DDC method, the displacement fluctuation of the motor can reach a degree approximate to the conventional control method. However, the DDC method does not need to solve the mathematical model online. The table of torque coefficient and suspension coefficient can be omitted in the program. This not only greatly shortens the interrupt time of the DSP controller, but also saves a lot of storage space and lightens the calculation burden of the DSP controller.
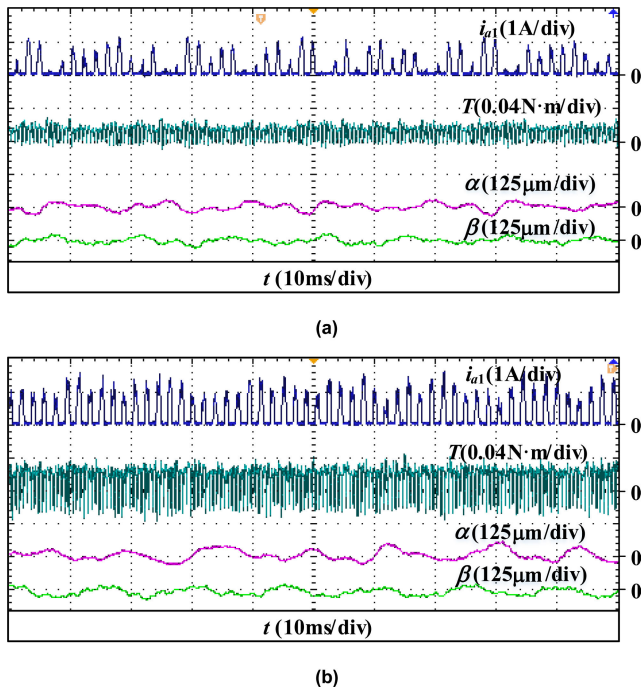
(a)

(b)

FIGURE 13. Experimental waveforms of winding current, torque and radial displacements. (a) Conventional control method. (b) DDC method.
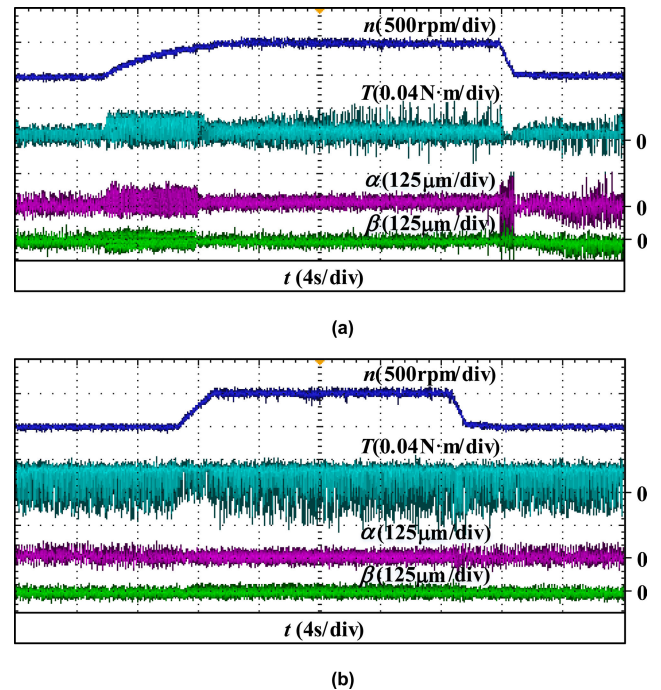

(a)

(b)

FIGURE 14. Experimental waveforms when speed increased from 2500 to 3000 r/min first and then decreased to 2500 r/min. (a) Conventional control method. (b) DDC method.

Fig. 13 shows experimental waveforms of winding current, torque and radial displacements at the speed of 4000 r/min with different methods. Under the conventional control method, the output torque is all positive. Because its torque conduction region is in the positive torque region $[-15°, 0°]$, the current is completely turned off in the negative torque region. Thus, no negative torque is generated in this method.

Under the DDC method, there is negative torque in the output torque. Because the output of the PI controller is the advanced angle θ_m. As long as θ_m has not reached saturation, each phase must be opened after $-15°$. Since the electrical cycle is $45°$, single-phase conduction is used, so the conduction region is still $15°$, so the turn-off angle must be greater. As a result, the current extends into the negative torque region, which generates negative torque.

B. DYNAMIC PERFORMANCE WITH THE DDC METHOD

In order to compare the dynamic performance of the conventional control method and the DDC method, a speed changing experiment was performed. In addition, a sudden knock experiment and a load changing experiment under the DDC method were also performed.

In the speed changing experiment, the speed was first increased from 2500 r/min to 3000 r/min, and then decreased to 2500 r/min. Fig. 14(a) shows the waveform of the speed changing under the conventional control method. It can be seen that the speed rise time is long, reaching 6s. In addition, the suspension displacement fluctuates greatly during the speed changing. This is because when the rotation speed is changed, the average exciting current I_m changes abruptly,

causing a sudden change in the suspension force. As a result, the levitation displacement fluctuates greatly. Fig. 14(b) shows the waveform of the speed changing under the DDC method. It can be seen that during the speed changing process, the displacement in the two directions has not changed, and the rotor is still very stable at the center of balance. This is because in the DDC method, the rotation speed is controlled by the lead angle. The advanced angle is updated once per inductor cycle and its update frequency is slow. As long as the response speed of the current difference loop is greater than the advanced angle update frequency, displacement control can be stabilized. The experimental results verify that the DDC method has better anti-disturbance than the conventional control method.

In the sudden knock experiment under the DDC method, the shaft was knocked at the direction of α axis and β axis, respectively. Fig. 15 shows waveforms of the sudden knock experiment at the speed of 2000 r/min. When the motor shaft was knocked in α direction, the rotating shaft was shifted. However, under the action of the displacement closed-loop, the rotating shaft generates a force opposite to the direction of knocking, and the rotating shaft is pulled back to the center of balance again, as shown in Fig. 15(a). Fig. 15(b) is the waveform of knocking the rotating shaft in the β direction, and the principle is consistent with α direction. This experiment also proves that the DDC strategy has a better anti-disturbance performance.

Fig. 16 $\sim$ Fig. 18 shows the experimental waveform of the load changing experiment under the DDC method. During the load-changing process, the sponge can be used to rub the
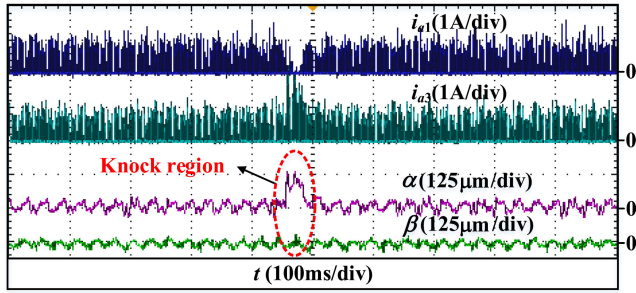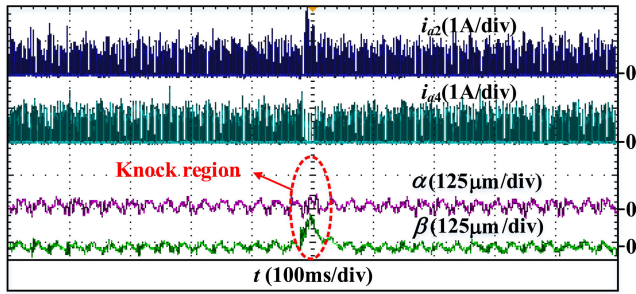
FIGURE 15. Experimental waveforms when knocking the shaft with the DDC method. (a) α direction. (b) β direction.
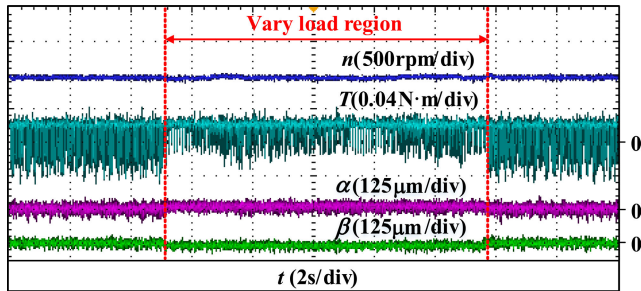

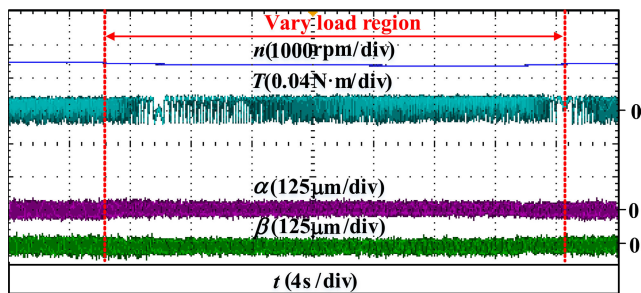**FIGURE 16.** Experimental waveforms when changing the load at the speed of 2000 r/min with the DDC method.

FIGURE 17. Experimental waveforms when changing the load at the speed of 1500 r/min with the DDC method.

FIGURE 18. Experimental waveforms when changing the load at the speed of 2500 r/min with the DDC method.

TABLE 2. Comparison of steady-state performance between the conventional method and the DDC method at the speed of 4000r/min

	Conventional control method	DDC method
RMS current of phase A (mA)	433	462
Torque ripple (N·m)	0.024	0.048
Levitation ripple in α-axis direction (μm)	35	35
Levitation ripple in β-axis direction (μm)	40	40
Algorithm execution time (μs)	16.8	10.7

TABLE 3. Comparison of dynamic performance between the conventional method and the DDC method

	Conventional control method	DDC method
Speed rise-time (s)	6	2.4
Speed fall-time (s)	1	0.8
Levitation ripple in α-axis direction when speed increases (μm)	100	40
Levitation ripple in α-axis direction when speed decreases (μm)	175	50
Levitation ripple in β-axis direction when speed increases (μm)	75	40
Levitation ripple in β-axis direction when speed decreases (μm)	150	40

rotor to increase the load torque. When the load increases, the conduction region shifts to the positive torque region, so that the output torque also increases to balance the load torque. When the load decreases, the conduction region shifts to the negative torque region, which generates negative torque
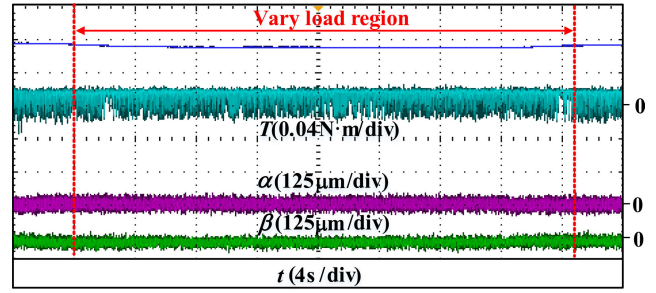
to reduce average torque. When the load changes, the speed and displacement are not affected. This also verifies that the DDC method has a good dynamic performance.

C. COMPARISON BETWEEN THE CONVENTIONAL CONTROL METHOD AND THE DDC METHOD

To analyze the advantages and disadvantages of the conventional control method and the DDC method, based on the above waveforms, the steady-state performance and the dynamic performance of the two methods are compared. Table 2 shows the comparison results of the steady-state performance experiment. Table 3 shows the comparison results of the dynamic performance experiment. Under steady-state experiments, the algorithm execution time of the DDC method is reduced by 36.3% compared with the conventional control method. Under dynamic experiments, compared with the conventional control method, the DDC method speed-up

time is reduced by 60%, and the speed-down time is reduced by 20%. At the same time, during the process of changing the speed, the displacement fluctuation under the DDC strategy remained basically unchanged.
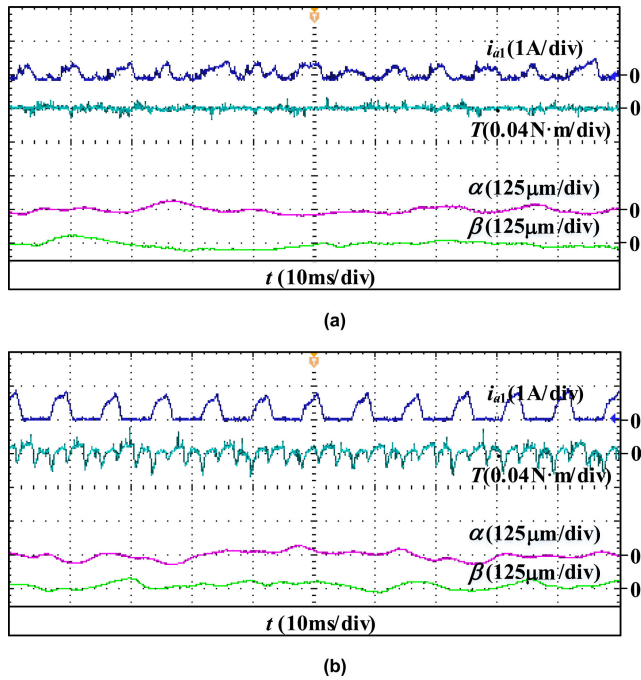

FIGURE 19. Experimental waveforms of winding current, torque and radial displacements at the speed of 1000 r/min. (a) DTC and DFC method. (b) DDC method.

D. COMPARISON BETWEEN THE DTC AND DFC METHOD AND THE DDC METHOD

Fig. 19 shows experimental waveforms of winding currents, torque and radial displacements at the speed of 1000 r/min with the DTC and DFC method and DDC method. Compared with DDC control strategy, it can be seen that the RMS current and torque ripple of the DTC strategy are significantly smaller than the DDC method, and the displacement fluctuation is also slightly smaller than the latter. Because the DTC and DFC method directly controls the torque and levitation force, and controls the three-phase instantaneous synthetic torque at the same time, while DDC method provides torque in a single phase, and the torque ripple in the commutation interval is large. The DTC and DFC method is a full-cycle control strategy, and the suspension force is provided by each phase in the $[-7.5°, 7.5°]$ region. The DDC method provide torque and levitation force at the same time, so the levitation force control performance is not as good as the DTC and DFC method, resulting in greater displacement fluctuations. Table 4 shows the comparison results of the steady-state performance experiment at the speed of 1000 r/min with the DTC and DFC method and the DDC method.

Fig. 20 shows experimental waveforms of the speed changing experiment with the DTC and DFC method and DDC method. In this experiment, the rotation speed was first

TABLE 4. Comparison of steady-state performance between the DTC and DFC method and the DDC method at the speed of 1000 r/min

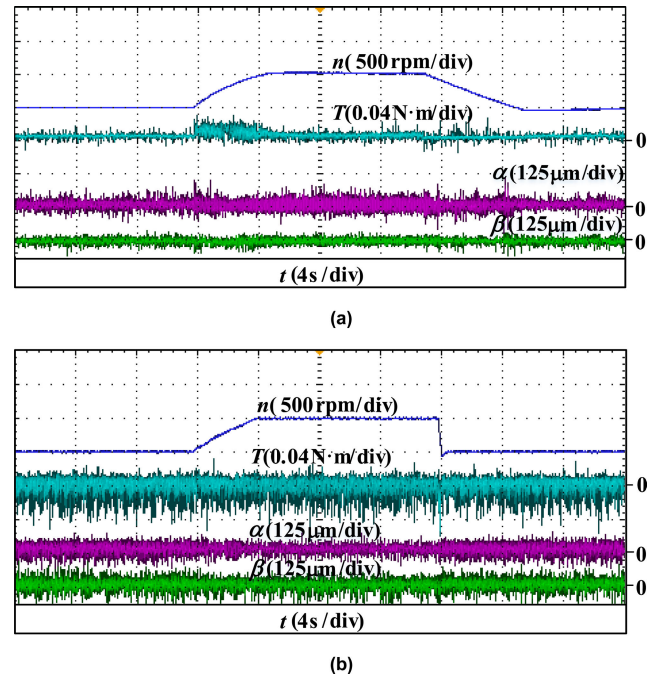|	DTC and DFC method	DDC method
RMS current of phase A (mA)	364	412
Torque ripple (N·m)	0.016	0.048
Levitation ripple in α-axis direction (μm)	25	35
Levitation ripple in β-axis direction (μm)	25	40
Algorithm execution time (μs)	18.2	10.7

FIGURE 20. Experimental waveforms when speed increased from 1000 to 1500 r/min first and then decreased to 1000 r/min. (a) DTC and DFC method. (b) DDC method.

increased from the original 1000 r/min to 1500 r/min with a certain slope, and then slowly decreased to 1000 r/min with the same slope. It can be seen that the displacement fluctuation of the DTC and DFC method becomes larger during the speed increase and decrease process, while the displacement fluctuation of the DDC strategy remains unchanged during the speed change process. Table 5 shows the comparison results of the dynamic performance experiment at the speed of 1000 r/min with the DTC and DFC method and the DDC method. Under dynamic experiments, compared with the DTC and DFC method, the DDC method speed-up time is reduced by 23%, and the speed-down time is reduced by 86.6%. Because the DTC method synthesizes the total torque through three-phase instantaneous torque. When increasing or decreasing the torque, the selection of the voltage vector also needs to consider the flux error signal. This causes the effect of the final synthetic torque to be affected, so that it takes a long time to increase and decrease speed. The DDC

TABLE 5. Comparison of dynamic performance between the DTC and DFC method and the DDC method

	DTC and DFC method	DDC method
Speed rise-time (s)	5.2	4
Speed fall-time (s)	6	0.8
Levitation ripple in α-axis direction when speed increases (μm)	100	75
Levitation ripple in α-axis direction when speed decreases (μm)	100	75
Levitation ripple in β-axis direction when speed increases (μm)	75	100
Levitation ripple in β-axis direction when speed decreases (μm)	75	100

method provides torque in a single phase, and through the advanced angle to control. The torque control is more direct, and the time required to increase and decrease speed is shorter.
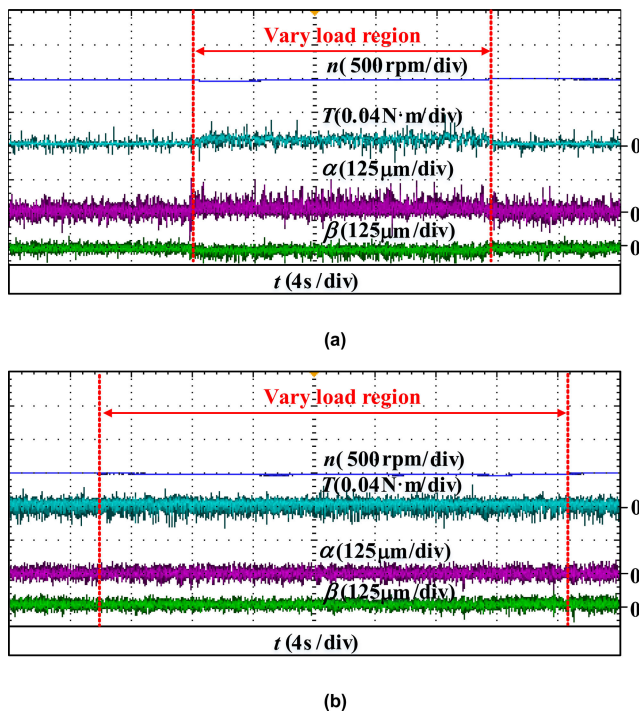

FIGURE 21. Experimental waveforms when changing the load at the speed of 1000 r/min. (a) DTC and DFC method. (b) DDC method.

Fig. 21 shows experimental waveforms of the load changing experiment with the DTC and DFC method and the DDC method. During the load-changing process, the sponge can be used to rub the rotor to increase the load torque. It can be seen that the displacement fluctuation of the DTC and DFC method changes when the load is changed. And the displacement of the load changing experiment at different speeds with the DDC method remains stable.

The above comparisons between the DTC and DFC method also show that the DDC method has good dynamic performance, the radial displacement is not affected by the speed and load changes, and the torque and suspension force are decoupled.
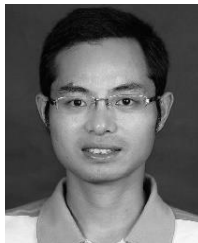
V. CONCLUSION
This paper studies a direct displacement control method for single winding BSRMs, which achieves rotor levitation by directly obtaining the current difference value through the closed-loop displacement. Meanwhile, the speed control is achieved by adjusting the advanced angle of phase conduction. Finally, the steady-state and dynamic experiments are compared between the proposed method and the conventional control method and the DTC and DFC method. Experimental results verify that the DDC method can still achieve the stable suspension of the rotor without model online calculation, and has good performance on the levitation control in the process of speed acceleration or deceleration and changing the load.

REFERENCES
[1] H. Chen, H. Yang, Y. Chen, and H. H.-C. Iu, "Reliability assessment of the switched reluctance motor drive under single switch chopping strategy," *IEEE Trans. Power Electron.*, vol. 31, no. 3, pp. 2395–2408, Mar. 2016.

[2] A. Chiba, K. Kiyota, N. Hoshi, M. Takemoto, and S. Ogasawara, "Development of a rare-earth-free SR motor with high torque density for hybrid vehicles," *IEEE Trans. Energy Convers.*, vol. 30, no. 1, pp. 175–182, Mar. 2015.

[3] J. Ye, B. Bilgin, and A. Emadi, "An extended-speed low-ripple torque control of switched reluctance motor drives," *IEEE Trans. Power Electron.*, vol. 30, no. 3, pp. 1457–1470, Mar. 2015.

[4] Z. Q. Zhu, B. Lee, L. Huang, and W. Chu, "Contribution of current harmonics to average torque and torque ripple in switched reluctance machines," *IEEE Trans. Magn.*, vol. 53, no. 3, pp. 1–9, Mar. 2017.

[5] S. Song, M. Zhang, and L. Ge, "A new fast method for obtaining flux-linkage characteristics of SRM," *IEEE Trans. Ind. Electron.*, vol. 62, no. 7, pp. 4105–4117, Jul. 2015.

[6] A. Chiba, T. Fukao, O. Ichikawa, M. Oshima, M. Takemoto, and D. Dorrell, *Magnetic Bearings and Bearingless Drives*. Amsterdam, The Netherlands: Elsevier, 2005.

[7] L. Chen and W. Hofmann, "Speed regulation technique of one bearingless 8/6 switched reluctance motor with simpler single winding structure," *IEEE Trans. Ind. Electron.*, vol. 59, no. 6, pp. 2592–2600, Jun. 2012, doi: 10.1109/TIE.2011.2163289.

[8] Y. Sun, X. Liu, D. Wang, and J. Mao, "Extension of mathematical model to full angle for bearingless switched reluctance motors based on finite-element analysis," (in Chinese), *Trans. China Electrotech. Soc.*, vol. 22, no. 9, pp. 34–39, 2007.

[9] M. Takemoto, A. Chiba, H. Akagi, and T. Fukao, "Radial force and torque of a bearingless switched reluctance motor operating in a region of magnetic saturation," *IEEE Trans. Ind. Appl.*, vol. 40, no. 1, pp. 103–112, Jan. 2004.

[10] M. Takemoto, A. Chiba, and T. Fukao, "A method of determining the advanced angle of square-wave currents in a bearingless switched reluctance motor," *IEEE Trans. Ind. Appl.*, vol. 37, no. 6, pp. 1702–1709, 2001.

[11] X. Cao, Z. Deng, G. Yang, and X. Wang, "Independent control of average torque and radial force in bearingless switched-reluctance motors with hybrid excitations," *IEEE Trans. Power Electron.*, vol. 24, no. 5, pp. 1376–1385, May 2009.

[12] J. Zhang, H. Wang, S. Zhu, C. Tan, and Y. Wang, "Multi-objective optimization of current waveform of bearingless switched reluctance motor for torque ripple and radial force ripple reduction," in *Proc. 14th IEEE Conf. Ind. Electron. Appl. (ICIEA)*, Xi'an, China, Jun. 2019, pp. 424–428, doi: 10.1109/ICIEA.2019.8833876.

[13] A. D. Cheok and Y. Fukuda, "A new torque and flux control method for switched reluctance motor drives," *IEEE Trans. Power Electron.*, vol. 17, no. 4, pp. 543–557, Jul. 2002.

[14] Q. Sun, X. Cao, and Z. Deng, "Direct torque and force control for dual-winding bearingless switched reluctance motor," in *Proc. 17th Int. Conf. Electr. Mach. Syst. (ICEMS)*, Hangzhou, China, Oct. 2014, pp. 1875–1880.

[15] P. G. Barrass and B. C. Mecrow, "Flux and torque control of switched reluctance machines," *IEE Proc., Electr. Power Appl.*, vol. 145, no. 6, pp. 519–527, Nov. 1998.

[16] X. Cao, J. Zhou, C. Liu, and Z. Deng, "Advanced control method for a single-winding bearingless switched reluctance motor to reduce torque ripple and radial displacement," *IEEE Trans. Energy Convers.*, vol. 32, no. 4, pp. 1533–1543, Dec. 2017.

[17] Q. Yu and X. Cao, "Hysteresis control of torque and levitation force for dual-winding bearingless switched reluctance motor," in *Proc. 14th IEEE Conf. Ind. Electron. Appl. (ICIEA)*, Xi'an, China, Jun. 2019, pp. 1173–1178.

[18] X. Cao, H. Yang, L. Zhang, and Z. Deng, "Compensation strategy of levitation forces for single-winding bearingless switched reluctance motor with one winding total short circuited," *IEEE Trans. Ind. Electron.*, vol. 63, no. 9, pp. 5534–5546, Sep. 2016.

[19] L. Chen, H. Wang, J. Zhang, C. Tan, and Y. Wang, "Coordinated control strategy based on adjustable turn-off angle for bearingless switched reluctance motor," in *Proc. 13th IEEE Conf. Ind. Electron. Appl. (ICIEA)*, Wuhan, May 2018, pp. 724–729, doi: 10.1109/ICIEA.2018.8397808.

[20] Z. Hao, X. Cao, X. Deng, and X. Shen, "Novel bearingless switched reluctance motor with wide flat inductance region to simplify the control of torque and levitation force," *IEEE Trans. Energy Convers.*, vol. 35, no. 3, pp. 1278–1288, Sep. 2020, doi: 10.1109/TEC.2020.2983190.

[21] Y. Huang, F. Huang, Y. Yuan, F. Yang, and K. Xie, "Design and analysis of a novel bearingless segmented switched reluctance motor," *IEEE Access*, vol. 7, pp. 94342–94349, 2019, doi: 10.1109/ACCESS.2019.2927537.

[22] K. D. Bachovchin, J. F. Hoburg, and R. F. Post, "Stable levitation of a passive magnetic bearing," *IEEE Trans. Magn.*, vol. 49, no. 1, pp. 609–617, Jan. 2013, doi: 10.1109/TMAG.2012.2209123.

[23] A. Smirnov, N. Uzhegov, T. Sillanpää, J. Pyrhönen and O. Pyrhönen, "High-speed electrical machine with active magnetic bearing system optimization," *IEEE Trans. Ind. Electron.*, vol. 64, no. 12, pp. 9876–9885, Dec. 2017, doi: 10.1109/TIE.2017.2716875.

[24] T. Schuhmann, W. Hofmann, and R. Werner, "Improving operational performance of active magnetic bearings using Kalman filter and state feedback control," *IEEE Trans. Ind. Electron.*, vol. 59, no. 2, pp. 821–829, Feb. 2012, doi: 10.1109/TIE.2011.2161056.

TAO ZHU graduated in electrical engineering from Nanjing Normal University, in 2018. He is currently pursuing the master's degree in electrical engineering with the Nanjing University of Aeronautics and Astronautics, China.

His current research interest includes bearingless switched reluctance motors.

XIN CAO (Member, IEEE) received the B.Eng., M.Sc., and Ph.D. degrees in electrical engineering from the Nanjing University of Aeronautics and Astronautics, Nanjing, China, in 2003, 2006, and 2010, respectively.

Since 2011, he has been with the Nanjing University of Aeronautics and Astronautics. From June 2011 to September 2012, he was a Research Associate with the Department of Aeronautical and Automotive Engineering, Loughborough University, Loughborough, U.K. His current research interests include distributed generation and renewable energy, electric vehicles, switched reluctance motors, and magnetically levitated bearingless motors.

QIANG YU received the B.Eng. degree in electrical engineering from the Jiangsu University of Science and Technology, Zhenjiang, in 2017, and the M.Sc. degree in electrical engineering from the Nanjing University of Aeronautics and Astronautics, Nanjing, China, in 2020. His current research interest includes bearingless switched reluctance motors.

ZHENYANG HAO (Member, IEEE) received the bachelor's degree in electrical engineering from Nanjing Normal University, in 2004, and the master's and Ph.D. degrees in power electronics and motion drive from the Nanjing University of Aeronautics and Astronautics, in 2010.

Since 2013, he has been an Associate Professor with the Department of Electrical Engineering, Nanjing University of Aeronautics and Astronautics. His research interests include new energy power electronic conversion technology, aviation power supply, power actuator technology, electric vehicle motor design, and driving technology.

QIYAO ZHANG (Student Member, IEEE) graduated in electrical engineering and automation from the Nanjing University of Aeronautics and Astronautics, China, in 2020, where she is currently pursuing the master's degree in electrical engineering. Her main research interest includes motor control.

• • •